Investigation of Fatigue Damage of Tempered Martensitic Steel during High Cycle Fatigue and Very High Cycle Fatigue Loading Using In Situ Monitoring by Scanning Electron Microscope and High-Resolution Thermography

*Alexander Giertler and Ulrich Krupp**

Dedicated to Prof. Dr.-Ing. Wolfgang Bleck on the occasion of his 70th birthday

Herein, the fatigue damage mechanisms of a low-alloyed 0.5 wt% carbon steel (50CrMo4) are examined in the high cycle fatigue and very high cycle fatigue regime, taking into account different strength conditions. For this purpose, the heat treatment of the material is conducted using two different batches at two different tempering temperatures, which lead to hardnesses of 37HRC and 57HRC, respectively. The fatigue tests are conducted accounting for different test frequencies of $f = 95$ Hz and $f = 20$ kHz, as well as size effects. It is found that the fatigue behavior of the tempered steel 50CrMo4 can be subdivided into type I (surface cracks) and type II (internal cracks) VHCF damage behavior depending on the material strength condition. With the aid of in situ test equipment, the influence of microstructural banding on the local fatigue strength is demonstrated by high-resolution thermography. By implementing an ultrasonic testing machine in a high-resolution scanning electron microscope, the development of a fine granular area (FGA) at an artificial defect in vacuum atmosphere is demonstrated.

1. Introduction

The prediction of the fatigue properties of modern engineering alloys is limited to a rather probabilistic approach that is due to a pronounced scatter in the high cycle fatigue (HCF) and very high cycle fatigue (VHCF) regime. Fabrication tolerances and light-weight-design requirements are reasons for a steadily increasing number of influence parameters that have to be considered in engineering design and dimensioning of components. These parameters include the microstructure of the material itself, that is, defects, such as nonmetallic inclusions, pores, oxides, and the material surface.[1,2] The link between these microstructural parameters and the fatigue damage process can be obtained, when it is possible to observe the respective interactions in one experiment.[3] Tempering steels obtain their particular mechanical properties by a two-stage heat treatment, consisting of normalizing, quenching, and tempering. Quenching the steel from austenitizing temperature to room temperature results in the diffusion-less martensite formation. The formation of martensite needles follows the microstructural relationship between face-centered cubic (fcc) austenite and body-centered tetragonal (bct) martensite needles according the Kurdjumow and Sachs' relationship.[4] The formation of the martensitic microstructure is not random but follows a strictly hierarchical setup in which the individual martensite laths are aligned within individual blocks. Several blocks of the same orientation in turn form a packet and several packets are located within a prior austenite grain.[5,6] A modification of the tempering temperature following the quenching process makes it possible to adjust the desired combination of strength and toughness in a targeted manner. Increasing the temperature leads to a decrease in the tetragonal distortion of the carbon-supersaturated bct lattice and to an increase in the size of the $(Fe,Cr)_3C$ carbide precipitates. In accordance to the relationship between the tempering treatment conditions and the hardness and static strength values from the tensile test, the fatigue strength of martensitic steels in the VHCF regime increases with decreasing tempering temperature.[7] However, the effect on the fatigue mechanism and the fatigue limit in the VCHF regime ($N_{fracture} > 10^7$ cycles) is rather complex. The VHCF fatigue behavior can be divided into a type I

A. Giertler
Institute of Materials Design and Structural Integrity
University of Applied Sciences Osnabrück
49009 Osnabrück, Germany

U. Krupp
IEHK Steel Institute
RWTH Aachen University
Intzestraße 1, 52072 Aachen, Germany
E-mail: krupp@iehk.rwth-aachen.de

and a type II mechanism.[8] The type I behavior describes the initiation of surface cracks by the formation and growth of persistent slip bands (PSBs) caused by accumulated local plastic cyclic deformation. The formation of PSBs leads to a localized stress build-up within the microstructure, which, when high enough, causes fatigue crack initiation. The subsequent fatigue crack propagation depends on the local barrier strength of the microstructure, where microstructural features, such as prior austenite grain boundaries or martensite packet boundaries,[9] can act as an effective barrier against slip band transmission and fatigue crack growth. Eventually, these barriers slow down or stop crack propagation.[10] In contrast, type II fatigue behavior refers to internal crack initiation in the bulk at nonmetallic inclusions or grain boundary arrangements that cause high anisotropy stresses. Internal type II crack initiation can be observed predominantly in high-strength steels.[11,12] Here, with decreasing stress amplitude and thus extended fatigue life, the formation of a fine granular area (FGA) on the fracture surface in direct proximity to nonmetallic inclusions can be observed. Prerequisite of the FGA is the stress concentration at the inclusion, leading to a substantial amount of accumulated plastic strain. Dislocation patterning leads to polygonization and nanograin formation. A local grain refining of the microstructure due to the high dislocation density prevailing in the martensitic microstructure, high remote stress amplitude, and correspondingly high VHCF load cycles occurs. The local grain refinement leads to a local reduction of the threshold value of the cyclic stress intensity factor for fatigue crack initiation and thus promotes crack initiation.[12–14]

2. Experimental Section

2.1. Material

The study aims at the quantification of the influence of different material conditions on the fatigue behavior of the low-alloy tempered steel 50CrMo4 (German designation: 1.7228). The chemical composition of the material is shown in **Table 1**. The mechanical properties of the steel were adjusted by a two-stage heat treatment. For this purpose, round bar sections were austenitized at a temperature of 860 °C and then quenched in oil. By changing the tempering temperature, the hardness and strength of tempered steels were adjusted. Within the scope of the work, two different tempering temperatures of 200 and 550 °C each for 90 min were used, resulting in two different material conditions with a hardness of 57HRC and 37HRC.

Table 1. Chemical composition (wt%) for the steel 50CrMo4.

C	Cr	Mo	Mn	Fe
0.48	1.00	0.18	0.71	bal.

Table 2. Mechanical properties for the steel 50CrMo4.

HRC	$R_{p0,2}$ [MPa]	R_m [MPa]
37	992	1095
57	1561	2128
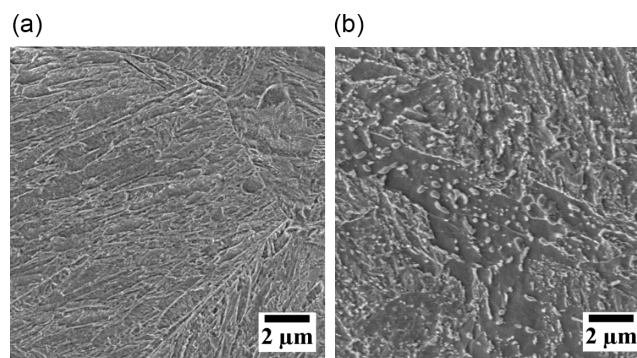
Figure 1. Microstructure of 50CrMo4 steel transverse to rolling direction: a) tempered at 200 °C and b) tempered at 550 °C.

The quasistatic mechanical properties obtained by the uniaxial tensile test for the two material conditions are shown in **Table 2**. The lower tempering temperature led to a higher strength and hardness of 57HRC, whereas the decrease in strength and hardness to 37HRC was attributed to the higher tempering temperature.

A comparison of the microstructures resulting from the heat treatments of the material is shown in **Figure 1**. While in the 200 °C-tempered condition no carbides were visible in the scanning electron microscope (SEM) micrograph, the higher tempering temperature led to a pronounced carbide precipitation (size up to ≈200 nm). In addition to the metallographic investigations, the microstructure of the material was investigated with the aid of automated electron backscattering diffraction (EBSD). A statistical evaluation of the crystallographic orientations did not show any texture evidence of a preferential orientation along the rolling direction in the hot-rolled steel.

With the aid of the crystallographic orientation data obtained by the EBSD measurements (see Figure 6), a reconstruction of the former austenite grains by the software ARPGE became possible.[15] The reconstruction of the prior austenite grains with a mean grain size of 14 μm showed that the martensitic transformation during quenching followed strictly the orientation relationship according to Kurdjumow–Sachs' $\{111\}_A\|\{011\}_M$ $\langle110\rangle_A\|\langle111\rangle_M$.

2.2. Fatigue Testing

Cylindrical fatigue specimens were machined from the heat-treated bars. The surfaces of the fatigue specimens were polished mechanically, as well as electrolytically to allow in situ monitoring of the fatigue damage on the surface of the specimens during the fatigue tests and correlate these observations with EBSD measurements of the crystallographic orientation distribution. A shallow notch with a notch factor of 1.2 was machined in the gauge length of the fatigue specimens with a hardness of 37HRC. The shallow notch led to localization of the fatigue damage and enabled the in situ observation of the sample surface during fatigue testing with the aid of a high-resolution digital microscope, type HIROX, as well as a high-resolution thermographic camera, type Infratec ImagerIR 8380 hp, with a resolution of 1.9 μm and a temperature resolution < 0.02 K. The fatigue tests were conducted on a RUMUL Testronic 100kN resonant testing machine with a test frequency of $f = 95$ Hz and a stress

(a)

(b)
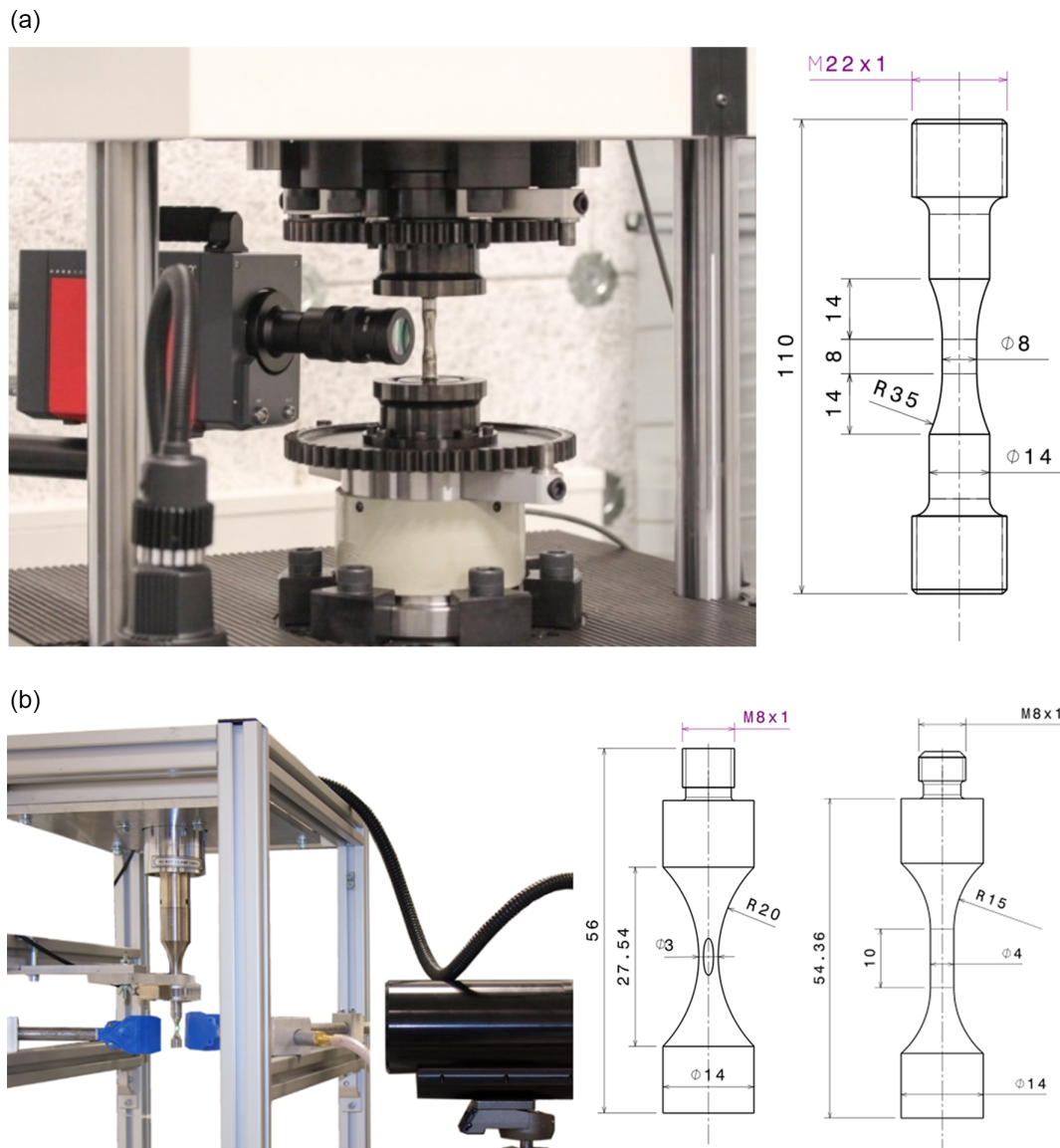
Figure 2. VHCF testing with respective specimen geometries: a) resonance testing machine with thermo camera and b) piezo-driven ultrasonic fatigue testing system with a light optical microscope (LOM).

ratio of $R = -1$, **Figure 2**a. In addition, fatigue tests were also conducted using an ultrasonic testing machine of the type BOKU Vienna with a test frequency of $f = 20$ kHz and a stress ratio of $R = -1$. To limit the temperature of the specimens during ultrasonic fatigue testing to $T_{specimen} < 40\,^{\circ}C$, air cooling and pulse-pause mode were used. For the 37HRC hardness condition, a pulse of 50 ms and a pause of 950 ms and for the 57HRC hardness condition, a pulse of 200 ms and a pause of 800 ms were applied. All experiments were conducted at room temperature in laboratory air atmosphere, Figure 2b.

Understanding the microstructural fatigue damage processes during fatigue loading required their observability. In the case of type II damage within the material volume, the damage process remained hidden. However, Spriestersbach et al.[16] showed that at artificial defects in vacuum atmosphere, the characteristic

damage mechanisms for type II fatigue behavior could also occur on the specimens' surface and thereby become observable. Therefore, to observe in situ the type II failure at the 57HRC material condition, artificial defects were introduced by focused ion beam (FIB) milling, implementing the ultrasonic testing machine into a ZEISS Auriga high-resolution SEM (**Figure 3**). All of the fatigued specimens were investigated using SEM in combination with automated EBSD, FIB, and energy-dispersive X-ray (EDX) analysis.

3. Results and Discussion

In the following, a distinction is made between type I and type II VHCF behaviors, with respect to the damage mechanisms

2100268 (3 of 9)

(a)

(b)
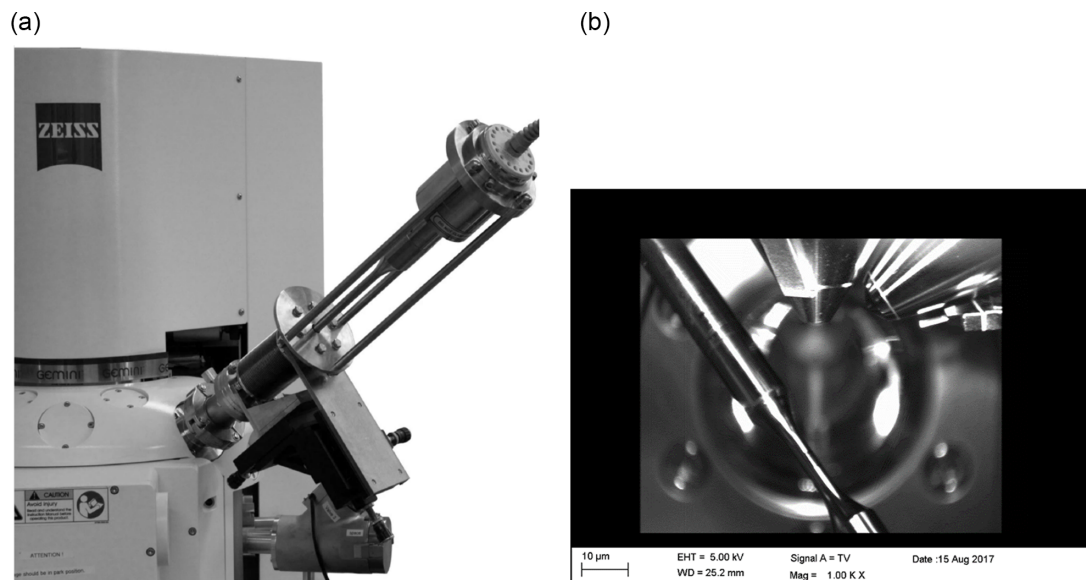
Figure 3. Implementation of an ultrasonic fatigue testing system in a high-resolution SEM: a) complete setup and b) view into the vacuum chamber of the SEM. The fatigue specimen is located below the pole piece. The ultrasonic wave is passed through an extension of the titanium horn through a vacuum seal in the SEM.

observed in the fatigue tests for the material conditions of 37HRC and 57HRC, respectively.

3.1. Type I Fatigue Behavior

The fatigue life stress vs. number of cycles (S–N) diagram for both test frequencies of 95 Hz and 20 kHz for the investigated material 50CrMo4 with a hardness of 37HRC is shown in **Figure 4**. During all tests, fatigue cracks were shown to initiate at the surface of the specimens and no internal crack initiation was observed. The fatigue limit (dashed horizontal lines in Figure 4) for the test frequency of $f = 95$ Hz is $\sigma_{FL} = 490$ MPa, and for the test frequency $f = 20$ kHz it is $\sigma_{FL} = 680$ MPa.
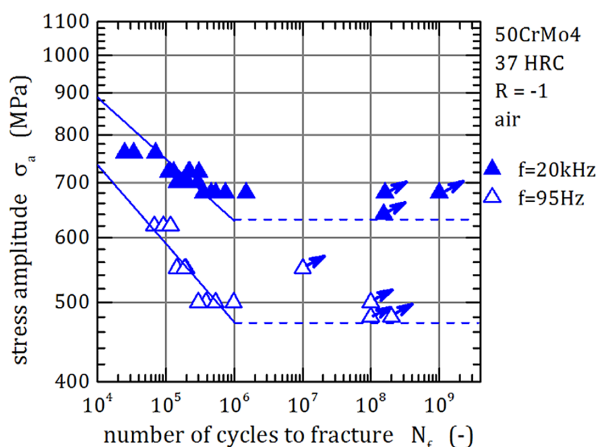

Figure 4. Wöhler S–N diagram showing the fatigue life for the steel 50CrMo4 at two testing frequencies of $f = 95$ Hz and $f = 20$ kHz for the 37HRC hardness condition.

The observed increase in fatigue strength with increasing test frequency is an often-observed characteristic of high-tempered steels.[17] The pronounced difference in fatigue strength of $\Delta\sigma = 200$ MPa for the 37HRC hardness condition can be attributed to an influence of the test frequency. An increase in the test frequency from $f = 95$ Hz to $f = 20$ kHz leads to a substantial increase in the strain rate during loading and unloading. The influence of the strain rate can be attributed to the well-known subdivision of the flow stress into an athermal σ_G and a thermal σ^* component.[18] The athermal fraction σ_G is independent of Peierls' stress and describes the stress proportion, which is necessary for moving dislocations to bow out and to overcome the elastic interaction with other dislocations (passing stress). The thermal component results from the thermal activation of Peierls' stress, necessary to allow screw dislocations to move at a given temperature and strain rate. According to the analysis by Seeger,[18] the thermal component is negligibly small above a transition temperature T_0 or below a transition strain rate $\dot{\varepsilon}_T$. Below the transition temperature T_0 or above the transition strain rate $\dot{\varepsilon}_T$, this component must be applied purely mechanically to activate plastic flow and therefore leads to higher fatigue strength values at higher test frequencies.

Figure 5 shows a thermograph of the sample surface during fatigue obtained by means of high-resolution thermography. After a certain incubation time, pronounced local plastic deformation in a band-like structure became evident. Crack initiation within a ribbon-like structure occurred.

The ribbon-like structure is developed, as a consequence of locally different plastic deformation. The reason for this is caused by microstructural banding, which has its origin in dendritic segregation during continuous casting process and the associated hot-rolling process in the steel mill, as shown in **Figure 6**. During solidification in the continuous casting process, the cooling rate in the core area is reduced to such an extent that
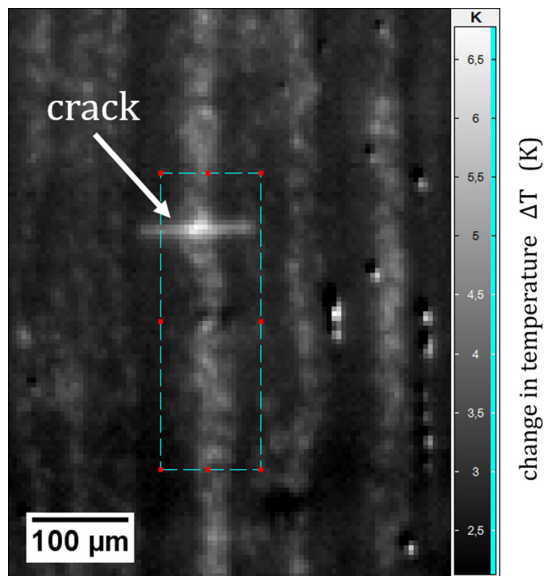
Figure 5. Surface of a fatigue specimen during cycling taken by means of high-resolution thermography at $N = 2.7 \times 10^6$ cycles loaded at $\sigma_a = 510$ MPa. The loading direction is parallel to the vertical direction of the image.
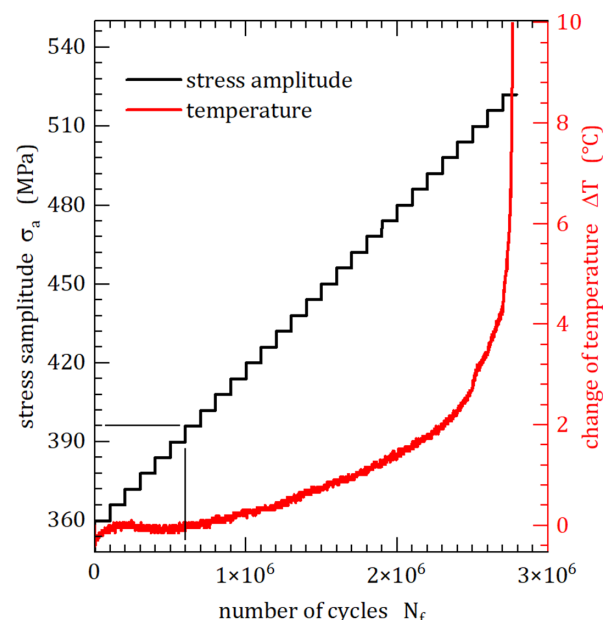
dendritic solidification occurs and as a result, the segregation of alloying elements cannot be prevented. EDX measurements have shown that areas with pronounced local plastic deformation (light areas in Figure 5) show a reduction in the Cr content by $\approx \Delta c_{Cr} = 0.2$ wt%. Furthermore, it was found by microhardness measurements that the hardness in Cr-depleted areas is reduced, which is obviously the reason for the localization of plastic deformation.
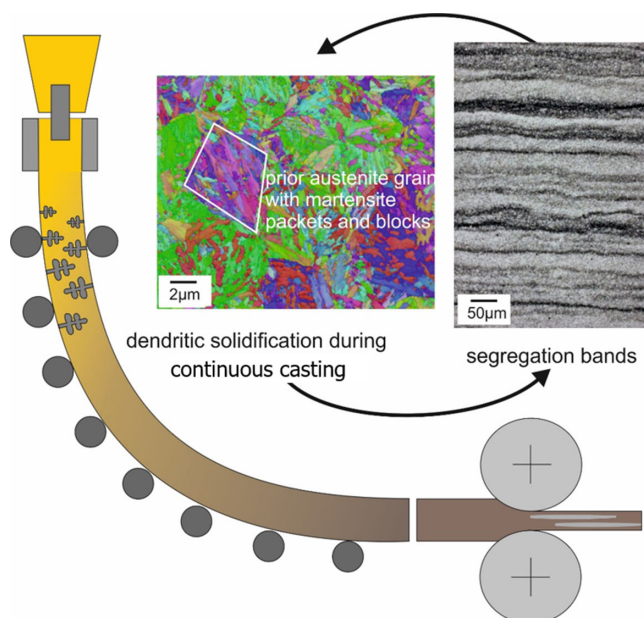
Considering the crack propagation in Figure 5, it becomes evident that the crack grows alternately through areas with already existing fatigue damage by local plastic deformation and through areas without damage. Load increase tests have been conducted in the resonance fatigue testing machine to understand the relationship between local plastic deformation and the macroscopic fatigue behavior, see **Figure 7**. The load increase test starts with a stress amplitude of $\sigma_a = 360$ MPa, which is far below the macroscopic yield strength of the material, see Table 2. The stress amplitude is stepwise increased during the test by 6 MPa every 100 000 cycles until fracture of the specimen occurs. The surface of the fatigue specimens was observed by a thermography camera, and every 1000 cycles, a thermogram was stored.

It is worth mentioning that a continuous increase in the temperature sets in when reaching a stress amplitude of $\sigma_a = 396$ MPa (after about 600 000 cycles in Figure 7). As the temperature increase can be correlated with the energy dissipation due to irreversible plastic slip, while the stress amplitude is far below the macroscopic yield strength and even below the fatigue limit ($\sigma_{FL} = 490$ MPa, see Figure 4), one can conclude that "infinite" fatigue life (in a technical sense up to 10^9 cycles) might be possible even when plastic slip is active. This is supported by SEM investigations of run-out specimens from fatigue tests, see **Figure 8**, showing irreversible fatigue damage in the form of local plastic deformation. In this case, it was possible to identify locations with already-existing microcracks by means of FIB sectioning.[9] Against this background, it can be concluded that the barrier effect of the microstructure was sufficiently high to prevent crack growth up to 10^9 cycles. This may change when load spectra with overload cycles have to be taken into account.


Figure 6. Schematic representation of the microstructure inhomogeneities resulting from the process steps' continuous casting, rolling, and heat treatment.

Figure 7. Stepwise load increase test, conducted in the resonance fatigue testing machine with $f = 95$ Hz: the specimen response is plotted as the change of temperature versus number of cycles.

2100268 (5 of 9)

(a)

(b)

Pt-coating

1 µm

500 nm
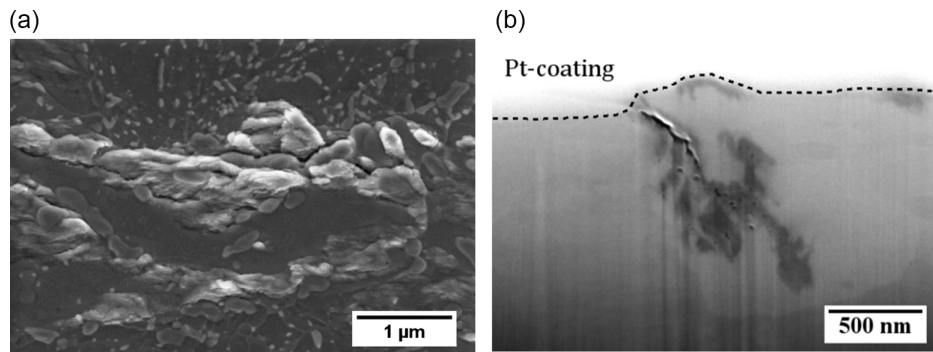
Figure 8. Run-out fatigue specimen after $N = 2 \times 10^8$ cycles loaded with a constant amplitude of $\sigma_a = 490$ MPa a) showing local plastic deformation (PSBs with extrusions) at the surface and b) respective FIB section through the crack shown in (a).

3.2. Type II Fatigue Behavior

In the case of the material condition of 57HRC, the data points shown in **Figure 9** correspond only to crack initiation at nonmetallic inclusions of the type Al_2O_3. As expected, the fatigue strength values are shifted to higher strength levels as compared with the material condition of 37HRC hardness. The only small deviation of the fatigue strength with increasing test frequency from $f = 95$ Hz to $f = 20$ kHz can be attributed in this case to a change of the testing machine and thus the change of the specimen geometry. By changing the specimen geometry, when changing from $f = 95$ Hz to $f = 20$ kHz, the critical volume within the gauge length of the sample geometry was reduced from $V_{95Hz} = 402$ mm³ to $V_{20kHz} = 125$ mm³; thereby, the probability of crack initiation on correspondingly large nonmetallic inclusions was reduced in addition, resulting in an improved fatigue life. This is supported by a statistical evaluation of the critical defect size on the fracture surfaces for the frequencies of $f = 95$ Hz and $f = 20$ kHz. The critical inclusion size is reduced from $A_{95Hz} = 700 \pm 200$ µm² for $f = 95$ Hz to $A_{20kHz} = 412 \pm 147$ µm² for 20 kHz. This can be attributed to the lower stochastic probability of large defects in the smaller gage volume of the 20 kHz samples. A pronounced frequency/strain-rate effect as in the case of the 37HRC condition was not observed, as it is supported by the fracture mechanical evaluation of the failure behavior, see Figure 12, where both, the 95 Hz and 20 kHz experiments, are in line for the calculation of the stress-intensity factors.

As mentioned earlier, all fatigue specimens of condition 57HRC failed by internal crack initiation (type II behavior). A characteristic feature is the so-called "fish-eye," which can be observed on the fracture surfaces of the fatigue specimens, see **Figure 10**. Crack initiation occurs in the centre of the fish-eye, whereas the outer circle separates the area of stable fatigue crack propagation (da/dN vs. ΔK follows the Paris law) and rupture of the residual cross section. That means, when the fish-eye crack has reached a critical size, unstable crack propagation outside the fish-eye sets in ($K_{max} > K_{Ic}$), followed by the fracture of the specimen. In the centre of the fish-eye nonmetallic inclusions of the type Al_2O_3 were identified. Characteristic
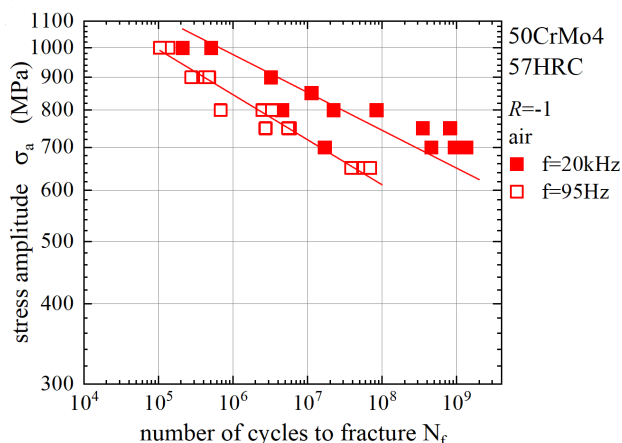
Figure 9. Wöhler S−N diagram showing the fatigue life for the steel 50CrMo4 at two testing frequencies of $f = 95$ Hz and $f = 20$ kHz for the 57HRC hardness condition.
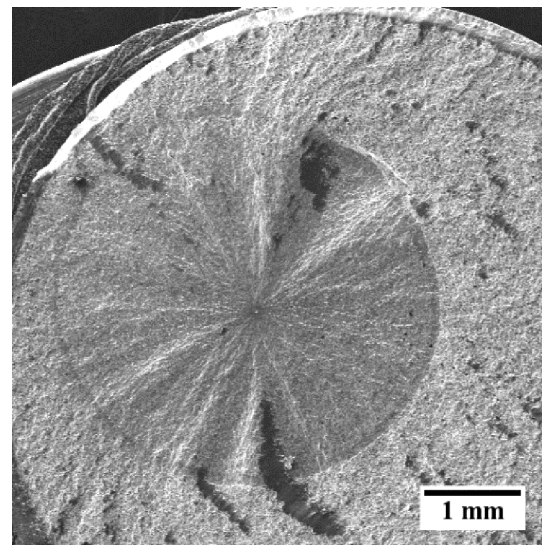
**Figure 10.** Internal crack initiation (fish-eye formation) at a nonmetallic Al_2O_3 inclusion and FGA formation on a fracture surface after $N_f = 2.7 \times 10^6$ number of cycles loaded with a stress amplitude of $\sigma_a = 750$ MPa.

are the conical cavities around the inclusions caused by the hot-rolling process. In direct proximity to the nonmetallic inclusions, the formation of an FGA can be observed, the size of which being a function of the stress amplitude σ_a, see **Figure 11** and **12**. According to Sakai[12] and Grad et al.,[13] the FGA is a result of accumulated cyclic microplasticity in the vicinity of the inclusion, leading at first to dislocation patterning, polygonization, and further on to nanograin formation. For the fracture mechanics assessment of the inclusions, the projection of the inclusion
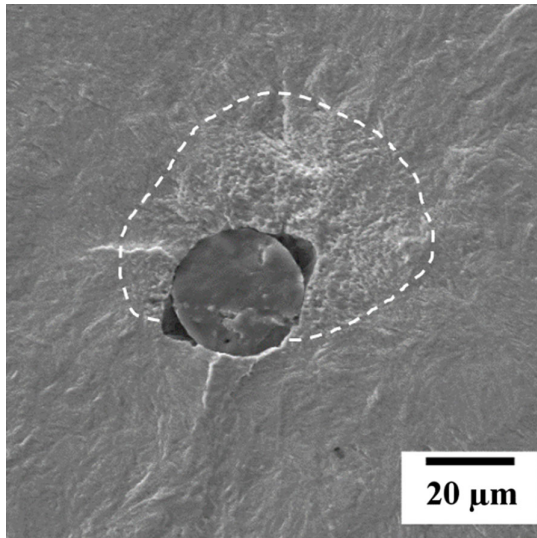
Figure 11. Internal crack initiation at a nonmetallic Al_2O_3 inclusion and FGA formation on a fracture (white dotted line) surface after $N_f = 5.7 \times 10^7$ number of cycles loaded with a stress amplitude of $\sigma_a = 650$ MPa.
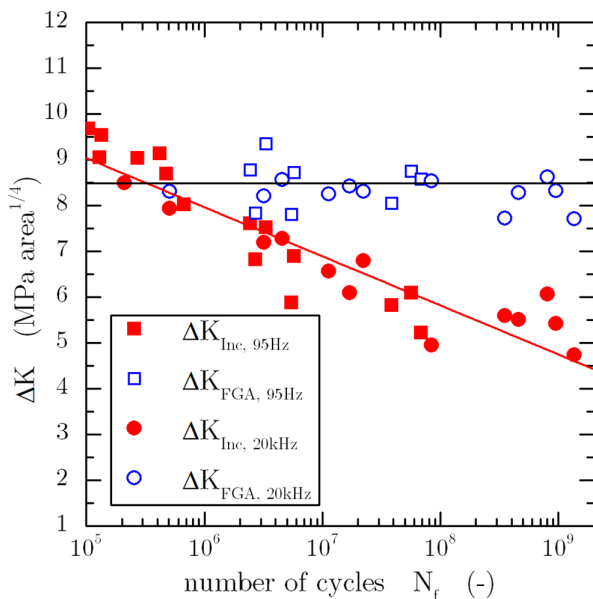
Figure 12. Calculation of the stress intensity factor ΔK for the nonmetallic inclusions and the corresponding FGAs based on the model according to Murakami.

size on a plane including the conical cavities according to the $\sqrt{area}$ principle is used.[19] Using Murakami`s approach,[20] the cyclic stress intensity factor range ΔK can be calculated using the following equation, taking into account the $\sqrt{area}$ principle for the inclusions and the FGAs.

$$\Delta K = 0.5 \Delta \sigma \sqrt{\pi \sqrt{area}} \tag{1}$$

By applying Equation (1) to the nonmetallic inclusions as well as the FGAs, the respective individual cyclic stress intensity factor range ΔK can be plotted as a function of the number of cycles, see Figure 12. Due to a fixed average size of the nonmetallic inclusions, the cyclic stress intensity factor ΔK decreases with decreasing stress amplitude σ_a and thus extended fatigue life.
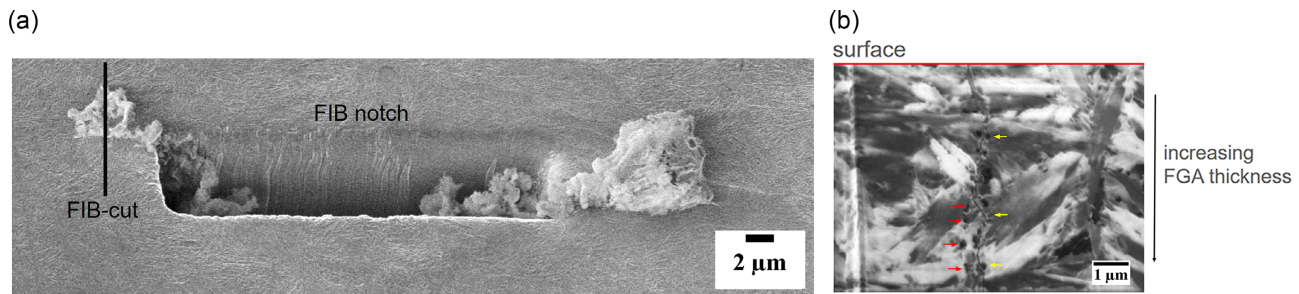
By means of fatigue crack growth analysis using single-edge-notched bend (SENB) specimens (according to ASTM E647), the threshold of the cyclic stress intensity factor $\Delta K_{th} = 9.5$ MPa$\sqrt{m}$ was determined in a previous investigation. A comparison with the data shown in Figure 12 shows that the values for ΔK determined for the inclusions alone in the VHCF regime are far below ΔK_{th}. Only by taking into account the transient formation of the FGA, technical fatigue crack initiation and crack propagation near the nonmetallic inclusions become possible. Hence, the FGA bridges the required stress intensity at the crack tip until the extension of the crack size (inclusion + FGA) at a given stress amplitude approaches $\approx \Delta K_{th}$.

To study the role of FGA formation during type II VHCF damage in detail, in situ experiments have been conducted with the aid of the ultrasonic testing machine in the SEM. The aim was to track FGA formation on artificial defects inserted by FIB milling in the SEM under vacuum conditions at the surface of the fatigue specimen (**Figure 13**). Subsequent investigation by targeted FIB sections revealed the formation and evolution of an FGA after 10^8 cycles (Figure 13b). Here, it is worth mentioning that 1) nanograins can be identified on both flanks of the propagating crack and 2) the thickness of the FGA (marked by the arrows in Figure 13b) increases with increasing crack depth. This is in accordance with the hypothesis that the grain refinement process is driven by the crack tip plastic zone r_p, which increases when the crack propagates.[16]

$$r_p = \frac{\pi}{8} \left(\frac{K_I}{\sigma_{ys}} \right) \tag{2}$$

Figure 14 shows the proposed FGA formation mechanism, that is, stress concentration at a nonmetallic inclusion, accumulated plasticity, dislocation patterning and polygonization, and eased crack initiation in the nanograined microstructure, as the threshold value for crack initiation in a nanograined microstructure ΔK_{FGA} is substantially smaller than the threshold value for the bulk material ΔK_{th}. During crack propagation, new nanograins are formed within the plastic zone ahead of the crack tip until the conditions for technical crack initiation, that is, $\Delta K = \Delta K_{th}$, are reached. Then, the crack propagates within the fish-eye until unstable crack propagation (fracture) occurs when K_{max} reaches the fracture toughness K_{Ic}.

2100268 (7 of 9)

**ADVANCED
SCIENCE NEWS**

www.advancedsciencenews.com

**steel
research**
international

www.steel-research.de

Figure 13. Crack initiation at artificial notch (FIB) after 10^8 cycles at $\sigma_a = 750$ MPa: a) surface cracks at the tips of the notch with pronounced extrusion and b) FIB section showing FGA formation at both sides of the crack flanks (red and yellow arrows).
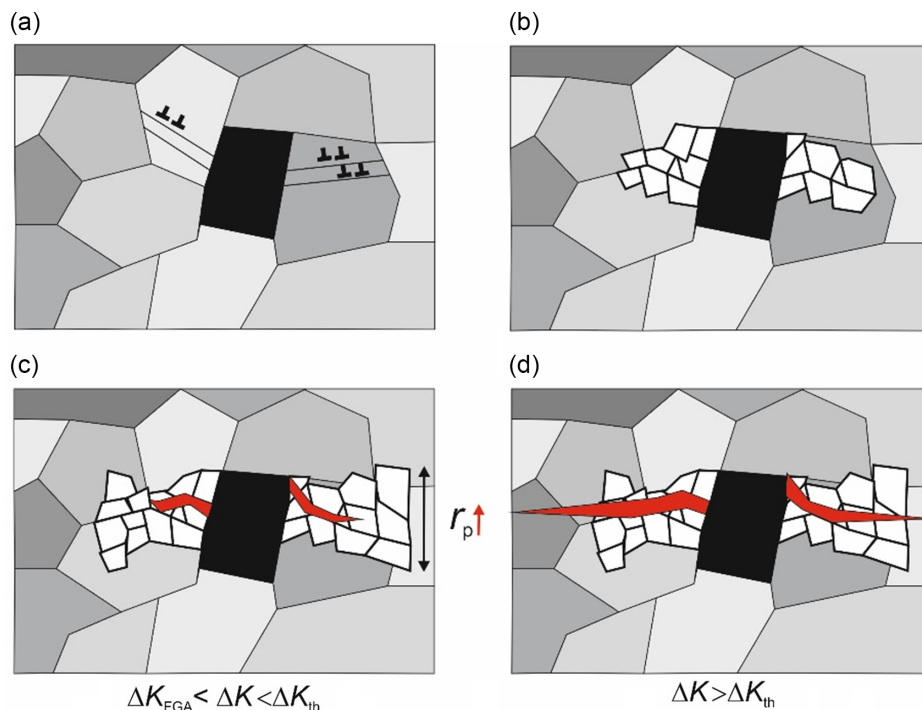
Figure 14. Schematic representation of FGA formation: a) stress concentration and plastic slip accumulation at inclusion, b) polygonization and nanograin formation, c) FGA crack initiation, and d) technical crack initiation.

4. Conclusion

The fatigue behavior in the VHCF regime of the steel 50CrMo4 was examined as a function of the strength condition as well as the test frequency. As expected, increasing fatigue strength was observed with increasing material strength from 37HRC to 57HRC. Here, however, a change in the damage behavior was observed. While the 37HRC fatigue specimens showed only surface crack initiation, the samples for 57HRC failed exclusively by crack initiation in the bulk at nonmetallic inclusions. Accordingly, the distinction of the VHCF fatigue behavior in type I or type II is dependent not only on the material, but also on the material condition. In addition, a pronounced influence of the test frequency on the fatigue tests for the material state 37HRC was observed. The change of the test frequency from $f = 95$ Hz to the test frequency of $f = 20$ kHz resulted in

fatigue strength (fatigue limit) increase of $\Delta\sigma_{FL} = 200$ MPa. High-resolution in situ thermography measurements contributed to the identification of metallurgical and mechanical properties that are inhomogeneously distributed at the microstructural level. The failure of the material condition of 37HRC hardness is characterized by the formation of persistant slip bands on the surface of the material due to local irreversible plastic deformation. Microcracks form along the slip bands, whereby the growth of microcracks is eventually prevented by the barrier effect of the surrounding microstructure. Taking into account the observed barrier effect of the martensitic microstructure at constant stress amplitude, the existence of a real fatigue limit for this material condition in the VHCF regime (in this study up to 10^9 cycles) is supported. In contrast, the material condition of 57HRC shows a higher fatigue strength, but these values continuously decrease with decreasing stress amplitude.

2100268 (8 of 9)

**ADVANCED
SCIENCE NEWS**

www.advancedsciencenews.com

**steel
research**
international

www.steel-research.de

Furthermore, in this case, the internal crack initiation on non-metallic inclusions dominates the fatigue life. With decreasing stress amplitude and therefore extended fatigue life, the formation of an FGA in the vicinity of nonmetallic inclusions was observed in the fracture surface. By applying Murakami's $\sqrt{area}$ approach, a fracture mechanical assessment of critical inclusion was conducted. In situ fatigue experiments in the SEM have confirmed that the formation of an FGA on artificial defects in vacuum atmosphere is possible. Finally, it was also shown that the test frequency, the volume size, and the material strength must be considered as influencing factors when determining the fatigue strength of a material.

Conflict of Interest

The authors declare no conflict of interest.

Data Availability Statement

Research data are not shared.

Keywords

fine granular areas, in situ scanning electron microscope fatigue monitoring, tempered martensitic steels, thermography, very high cycle fatigue

[1] T. Kunio, M. Shimizu, K. Yamada, K. Sakura, T. Yamamoto, *Int. J. Fract.* **1981**, *17*, 111.
[2] W. Li, T. Sakai, M. Wakita, S. Mimura, *Int. J. Fatigue* **2014**, *60*, 48.
[3] A. Korda, Y. Mutoh, Y. Miyashita, T. Sadasue, S. L. Mannan, *Scr. Mater.* **2006**, *54*, 1835.
[4] G. Kurdjumow, G. Sachs, *Zeitschrift für Physik* **1930**, *64*, 325.
[5] H. Kitahara, R. Ueji, N. Tsuji, Y. Minamino, *Acta Mater.* **2006**, *54*, 1279
[6] S. Morito, X. Huang, T. Furuhara, T. Maki, N. Hansen, *Acta Mater.* **2006**, *54*, 5323.
[7] A. Zhao, J. Xie, C. Sun, Z. Lei, Y. Hong, *Int. J. Fatigue* **2012**, *38*, 46.
[8] H. Mughrabi, *Int. J. Fatigue* **2006**, *28*, 1501.
[9] K. Koschella, U. Krupp, *Int. J. Fatigue* **2019**, *124*, 113.
[10] T. Zhai, X. Jiang, J. Li, M. Garratt, G. Bray, *Int. J. Fatigue* **2005**, *27*, 1202.
[11] H. Mughrabi, *Fatigue Fract. Eng. Mater. Struct.* **2002**, *25*, 755.
[12] T. Sakai, *JMMP* **2009**, *3*, 425.
[13] P. Grad, B. Reuscher, A. Brodyanski, M. Kopnarski, E. Kerscher, *Scr. Mater.* **2012**, *67*, 838.
[14] U. Krupp, A. Giertler, K. Koschella, *Fatigue Fract. Eng. Mater. Struct.* **2017**, *40*, 1731.
[15] C. J. Cayron, *App. Crystallogr.* **2006**, *40*, 1183.
[16] D. Spriestersbach, A. Brodyanski, J. Lösch, M. Kopnarski, E. Kerscher, *Mater. Sci. Technol.* **2016**, *32*, 1111.
[17] T. Swarr, G. Krauss, *Metall. Trans. A* **1976**, *7*, 41.
[18] A. Seeger, *London, Edinburgh Dublin Philos. Mag. J. Sci.* **1954**, *45*, 771.
[19] Y. Murakami, S. Kodama, S. Konuma, *Int. J. Fatigue* **1998**, *11*, 291.
[20] Y. Murakami, *Eng. Fract. Mech.* **1985**, *22*, 101.